Journal of Materials Chemistry A

Accepted Manuscript

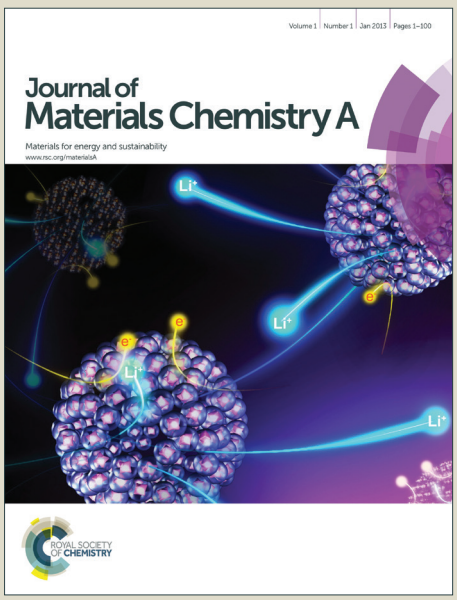

ROYAL SOCIETY OF CHEMISTRY

www.rsc.org/materialsA

Journal of Materials Chemistry A

Dynamic Article Links ►

Cite this: DOI: 10.1039/c0xx00000x

www.rsc.org/xxxxxx

ARTICLE TYPE

Graphene-Wrapped $Bi_2O_2CO_3$ Core-Shell Structures with Enhanced Quantum Efficiency Profit from Ultrafast Electron Transfer Process

Yalei Zhang,[*abc] Deyi Li,[abc] Yonggang Zhang,[*abc] Xuefei Zhou,[abc] Sujin Guo,[abc] Libin Yang,[abc]

Received (in XXX, XXX) Xth XXXXXXXXX 20XX, Accepted Xth XXXXXXXXX 20XX

DOI: 10.1039/b000000x

Graphene (GR) wrapped rose-liked $Bi_2O_2CO_3$ (WBGR) core/shell structures are synthesized to maximize their contact area and quantum efficiency. The Fourier Transform Infrared spectroscopy (FTIR) and X-ray photoelectron spectroscopy (XPS) results indicate that C-Bi bonds are formed, leading to a close chemical interfacial connection between $Bi_2O_2CO_3$ and GR as well as a concurrent a red shift at the absorption edge (λ = 430 nm). More importantly, an ultrafast electron transfer process (≤ 800 ps) from $Bi_2O_2CO_3$ to GR via C-Bi bonds is detected in the WBGR, inhibiting the recombination of the charge carriers and contributing to high photocatalytic activity during carbamazepine (CBZ) degradation. As a result, the highest the apparent quantum efficiency Φ (2.62%) and charge separation yield (9.4×10^{17} spin·g^{-1}) as well as quenching factor (4.51) is achieved on WBGR. Finally, radical control experiments demonstrate that the $\cdot O_2^-$ radicals, the ·OH radicals and the holes participated in the photocatalytic process. Consequently, WBGR displays the apparent rate constant (k) of $2.81\times10^{-4}\cdot s^{-1}$ and is 8.67 and 4.15-fold higher than $Bi_2O_2CO_3$ and graphene- $Bi_2O_2CO_3$ (BGR), respectively.

INTRODUCTION

Over the past two decades, bismuth-based nanostructured materials, such as Bi_2O_3,[1] $BiVO_4$,[2] Bi_2WO_6,[3] Bi_2MoO_6,[4, 5] BiOX (X=Cl, Br, I), and so on,[6-8] have received a great deal of attention due to their unique photocatalytic activities under visible-light. For instance, a new member of bismuth-containing materials, hierarchical $Bi_2O_2CO_3$, can be synthesized without template and deliver a promising visible-light photocatalytic performance.[9, 10] Furthermore, 3D hierarchical $Bi_2O_2CO_3$ architectures composed of 2D nanosheets or nanoplates are favorable for efficient reactant transport and photo-energy harvesting via the mesopores among the nanoplates and their high specific surface area. Regrettably, the quantum efficiency of individual $Bi_2O_2CO_3$ remains low due to the fast recombination of electron-hole pairs.[11, 12] In additional, the CB potential of $Bi_2O_2CO_3$ (0.15 V vs. NHE) is more positive than E_0 ($O_2/\cdot O_2^-$ =-0.28 V vs. NHE).[13] Therefore, there is no $\cdot O_2^-$ radical is produced, making the major active species the holes or the ·OH radicals during photocatalytic degradation.[14] Although it is a promising photocatalyst, the quantum efficiency of $Bi_2O_2CO_3$ should be further enhanced by coupling it with other matching materials during practical application.

Graphene (GR), as a two-dimensional carbon atom monolayer arranged in a honeycomb network, exhibits many unique properties, such as superior charge carrier mobility, high transparency, a large surface area, high thermal/chemical stabilities and excellent flexibility.[15, 16] Therefore, graphene (GR)-based semiconductor photocatalysts have attracted extensive attention since the discovery of GR in 2004.[17, 18] In addition, Xu et al. also report a thoughtful and inevitable comparison between GR- and its forebear carbon nanotube-based photocatalysts[19, 20] as well as demonstrate the new role of graphene as photosensitizer.[21] When GR is hybridized with other semiconductor oxides, the excellent electronic conductivity of GR promotes the transfer of photogenerated electrons through π-π bond interactions, inhibiting the recombination of the photoexcited electron-hole pairs.[22-24] Based on these unique properties of GR, Yu et al. have fabricated hierarchical graphene-$Bi_2O_2CO_3$ composites via template-free hydrothermal method to improve the quantum efficiency of $Bi_2O_2CO_3$.[25] However, the largest disadvantages of these composites are that only a small fraction area of $Bi_2O_2CO_3$ makes direct contact with the graphene, leading to relative low quantum efficiency as well as the $Bi_2O_2CO_3$ particles tend to agglomerate, decreasing the effective surface area during the photocatalytic degradation of

[a] *State Key Laboratory of Pollution Control and Resource Reuse, Tongji University, 1239 Siping Road, 200092 Shanghai, China. Tel: (0086) 021-65983803; Fax: (0086) 021-65985811; E-mail: zhangyalei@tongji.edu.cn*

[b] *Key Laboratory of Yangtze Water Environment of Ministry of Education. Tongji University, 1239 Siping Road, 200092 Shanghai, China. E-mail: zhouxeufei@tongji.edu.cn*

[c] *UNEP-Tongji Institute of Environment for Sustainable Development, Tongji University, 1239 Siping Road, 200092 Shanghai, China. E-mail: zhangyalei@tongji.edu.cn*

† Electronic Supplementary Information (ESI) available: [details of method description and additional Figures]. See DOI: 10.1039/b000000x/

organic pollutants.[26, 27] In order to overcome these disadvantages, an electrostatic self-assembly approach from Xu et al. and Park et al. is introduced.[28-31]

In this work, for the first time, we report on the fabrication of Graphene-wrapped $Bi_2O_2CO_3$ (WBGR) core/shell structures that highly enhance the quantum efficiency as well as photocatalytic activity of $Bi_2O_2CO_3$ via maximizing their contact area using graphene encapsulation. First, the graphene shell encapsulation not only inhibits the aggregation of the $Bi_2O_2CO_3$ microspheres but also protects them from structural destruction. Second, a slight red shift phenomenon at the $Bi_2O_2CO_3$ absorption edge is observed and is attributed to the formation of C-Bi bonds. More importantly, an ultrafast electron transfer process (≤ 800 ps) is detected via time-resolved photoluminescence (TRPL) spectroscopy,[32] indicating that the core-shell structures can promote photoexcited electron transfer from $Bi_2O_2CO_3$ to GR via chemical bonds interfacial interaction (C-Bi bonds). Specifically, quantum efficiency is investigated via the apparent quantum efficiency (Φ), charge separation yield and charge recombination rate. The electron paramagnetic resonance (EPR)[33] and photoluminescence (PL) spectroscopy results indicate that the ultrafast electron transfer process contributes to the highest charge separation yield (the trapped hole $\cdot O^-$ radical spin concentration is 9.4×10^{17} spin$\cdot g^{-1}$) and the lowest recombination rate (the quenching factor is 4.51) on WBGR. In additional, we also find that the electronic interaction and charge equilibration between GR and $Bi_2O_2CO_3$ shifts the E_F (from 0.25V vs. NHE to -0.27V vs. NHE) and decreases the CB potential (from 0.15V vs. NHE to -0.37 V vs. NHE, negative than $O_2/\cdot O_2^-$ =-0.28 V vs. NHE) of WBGR system during the photocatalytic experiment. Therefore, electrons from WBGR can react with O_2 to generate $\cdot O_2^-$ radicals that can then participate in the photocatalytic process. Finally, radical control experiments demonstrate that the $\cdot O_2^-$ radicals, the ·OH radicals and the holes participated in the photocatalytic process in WBGR. Consequently, WBGR displays the highest apparent rate constant ($2.81\times10^{-4}\cdot s^{-1}$) during CBZ degradation and is 8.67 and 4.15 times higher than that of the $Bi_2O_2CO_3$ and graphene-$Bi_2O_2CO_3$ (BGR), respectively. Furthermore, a correlation analysis between fast component lifetime constant (τ_1) and photocatalytic activity is discussed in the text.

EXPERIMENTAL SECTION

Materials

All of the reagents in this study are AR grade (Sigma Aldrich, Shanghai, China) and are used as received. Distilled water is used for all experiments.

Synthesis

The details of the synthesis of $Bi_2O_2CO_3$ hierarchical microspheres, graphene-$Bi_2O_2CO_3$ (BGR) and graphene-wrapped $Bi_2O_2CO_3$ microspheres (WBGR) are mentioned in Experiment section S1† and S2† of Supporting Information.

Characterization

The morphology of the photocatalyst is characterized using field emission environmental scanning electron microscopy (EFEG-SEM, Model Quanta 200 FEG, manufacturer FEI) and high-resolution TEM (Hitachi S-3000N). The crystal structure of the photocatalyst is characterized by using X-ray diffraction (XRD, Model D/max2550VB3+/PC, manufacture Rigaku). A Dilor LABRAM-1B microspectrometer is used to record the Raman spectra of the samples. Nitrogen adsorption-desorption isotherms are obtained with a nitrogen adsorption apparatus (ASAP 2020, USA). Chemical bonds formation is analyzed by Fourier transform infrared (FTIR) spectrometer (JASCO FT/IR-470, Japan) and X-ray photoelectron spectroscopy (XPS, Perkin Elmer PHI 5000 ESCA System with Al Kα radiation at 1486.6 eV)The optical absorption characteristics are determined with UV-visible diffuse reflectance spectroscopy (UV-vis DRS, Model BWS002, BWtek).

Photocatalytic degradation of carbamazepine (CBZ) and Radicals control experiment

The details of photocatalytic experiment and analytical method of CBZ are mentioned in Experiment S3† and S4† of supporting information.

Apparent quantum efficiency measurement

The apparent quantum efficiency for CBZ degradation can be calculated using eq 1:

$$\Phi = k / 2.303\, I_0\, \varepsilon_{D,\lambda}\, l \qquad (1)^{34}$$

Where Φ is the reaction of quantum yield (dimensionless), k is the photodegradation rate constant of CBZ during the photocatalytic test, I_0 is the light intensity of the incident light and the number of the incident photons is determined using a radiant power energy meter (2.18×10^{-6} Einstein L^{-1} S^{-1}), $\varepsilon_{D,\lambda}$ is the molar absorptivity of CBZ solution at 365 nm (4.27×10^3 cm^{-1} M^{-1}), l is the path length of reduction cell and is 5 cm for 100 mL of irradiated solution.

Electron Spin Resonance (EPR) Spectroscopy and $\cdot O_2^-$ radical Analysis

The details of EPR and $\cdot O_2^-$ radical experiments are mentioned in Experiment section S5† of supporting information.

Electrochemical measurements

The details are mentioned in Experiment section S6† of supporting information.

Photoluminescence (PL) and the time-resolved fluorescence spectra (TRPL)

The PL spectra are measured at room temperature using a Fluorescence Spectrophotometer (F-7000, Hitachi, Japan). The excitation wavelength is 365 nm. The time-resolved photoluminescence measurement is collected with a C5680 synchroscan streak camera (Hamamatsu, Japan). The test is carried out at 10 K with a 365 nm (3.4 eV) wavelength pulsed laser (Mira 900F, Coherent, USA) as an excitation source. The pulse width is approximately 6 ps. After the excitation, the sample emissions pass through a polarizer at a magic angle to the laser polarization to measure the isotropic fluorescence decay. The emission wavelength is measured according to PL spectrum. The temporal scanning ranges are selected as 2.5 and 200 ns, with IRF values as fast as 60 ps and 2 ns, respectively.[32] No transient signal is observed on GR under the same condition.

RESULTS AND DISCUSSION

Synthesis and Morphology

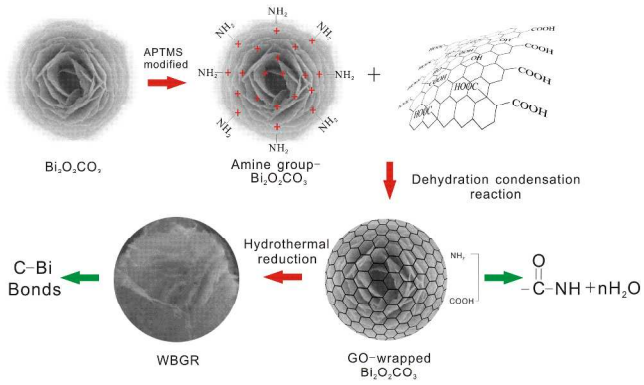

Scheme 1 Illustration of the preparation procedure for WBGR core/shell structure

The overall fabricating procedure for the WBGR core-shell structure microspheres is depicted in Scheme 1. First, the $Bi_2O_2CO_3$ microspheres are modified using 3-aminopropyltriethoxysilane (APTMS). Next, the positively charged $Bi_2O_2CO_3$ microspheres are wrapped by negatively charged GO via electrostatic interactions and direct chemical bonding reactions between the (-NH_2) groups on the $Bi_2O_2CO_3$ microspheres and the (-COOH) groups on GO. Finally, GO is reduced via hydrothermal treatment to obtain WBGR.

Fig. 1A displays an SEM image of the rose-shaped $Bi_2O_2CO_3$ microspheres. The average size of the microspheres is approximately 0.9 μm and they have a rough surface. The SEM with image higher magnification provided in Fig. 1B reveals that the 3D hierarchical architectures are composed of many layers of 2D nanoplates approximately 15nm thick; there are numerous nanopores in the microspheres. For the BGR, as observed in Fig. 1C, uniform $Bi_2O_2CO_3$ microspheres are anchored to the surface of the fully exfoliated, near-transparent GR. In contrast to that of the $Bi_2O_2CO_3$ and BGR, the surface of the WBGR (Fig. 1D) displays a wrinkled morphology, confirming that the $Bi_2O_2CO_3$ microspheres are wrapped by GR shells. To confirm the core-shell structure of WBGR more thoroughly, the WBGR are investigated using TME and HRTEM. Fig. 2A and B display the well-defined crystallinity of the $Bi_2O_2CO_3$ microspheres with a 0.271 nm lattice fringe ascribed to the (110) crystal plane of crystalline $Bi_2O_2CO_3$.[35] As observed in Fig. 2C, the $Bi_2O_2CO_3$ microspheres are coated by a GR shell approximately 5~10 nm thick.

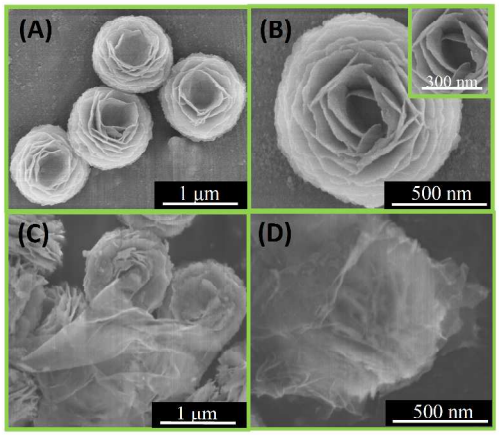

Fig. 1 SEM image of the as-prepared samples. **(A)** Low-magnification SEM image of $Bi_2O_2CO_3$. **(B)** High-magnification SEM image of $Bi_2O_2CO_3$.The insert shows the hierarchically structure with a resolution of 300 nm. **(C)** SEM image of BGR. **(D)** SEM image of WBGR.

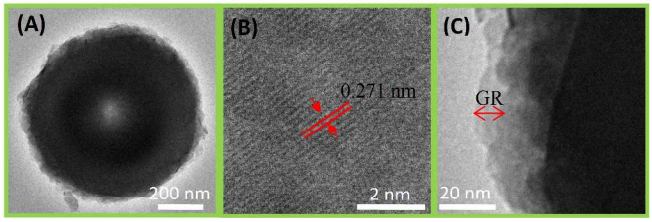

Fig. 2 TEM and HRTEM of the as-prepared samples (A). Low-magnification TEM image of WBGR. (B). High-magnification TEM image of WBGR. (C). TEM image of GR shell on WBGR.

The formation of C-Bi bonds

The structure and compositions of the WBGR are characterized by XRD and Raman spectroscopy (Fig. S1† and S2†). The Brunauer-Emmett-Teller (BET) surface is determined using the nitrogen adsorption-desorption isotherms (Fig. S3†). To understand the unique formation mechanism for the WBGR core/shell structure, the chemical bonds change (after GO-coating and the subsequent hydrothermal reduction process) is investigated using FTIR and XPS.

Fig. 3 presents the FTIR spectra of $Bi_2O_2CO_3$, BGR, and WBGR. For every sample, four typical internal vibration modes for CO_3^{2-} groups are observed including ν_1 (1067 cm^{-1}), ν_2 (846 cm^{-1}), ν_3 (1391 and 1468 cm^{-1}), ν_4 (670 cm^{-1}), respectively.[36] For BGR and WBGR, the absorption band at 1608 cm^{-1} reveals the skeletal vibration (C=C) of the GR.[27] Moreover, compared to the Bi-O-Bi (540 cm^{-1}) absorption band for $Bi_2O_2CO_3$ and BGR,[37] the absorption band for WBGR shifts toward a high wavenumber (600 cm^{-1}) and broadens. In addition, a new absorption band at 632 cm^{-1} is observed. The phenomenon is occurs mainly because the change of the chemical structure when carbon is present, resulting in a synergistic vibrational effect between the C-Bi and Bi-O-Bi bonds.[38] To confirm the formation of the C-Bi bonds, the XPS spectra are provided below.

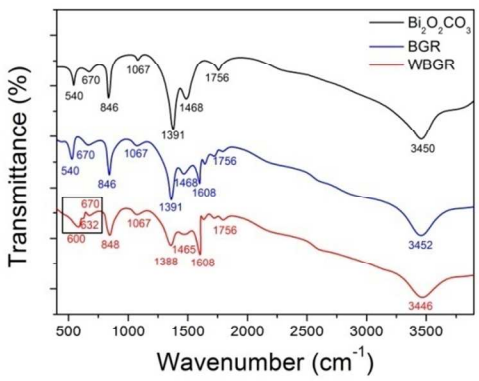

Fig.3 The FTIR spectra of $Bi_2O_2CO_3$, BGR and WBGR.

Fig. 4 displays the XPS spectra of the $Bi_2O_2CO_3$, BGR, and WBGR. In the C 1s spectra for $Bi_2O_2CO_3$, the peak at 284.8 eV is assigned to adventitious carbon species from XPS measurement, while the peak at 289.0 eV is assigned to the carbonate ion in $Bi_2O_2CO_3$.[9] Besides, for BGR and WBGR, the typical peaks located at 284.6 eV refer to the C=C-C bond in GR.[27] When comparing $Bi_2O_2CO_3$ and BGR, an additional shoulder-peak at 281.3 eV is observed for WBGR that is ascribed to the C-Bi bond (Scheme 2).[14] In addition, for WBGR, the C-N bond (285.8 eV) formed during the dehydration condensation chemical bonding reaction is apparent (Scheme 1).

The C-Bi bond formation can also be confirmed by analyzing the Bi 4f spectra. In the Bi 4f spectra of Fig.4 (D), two Bi 4f peaks at 158.8 and 164.1 eV are observed every sample and are ascribed to Bi $4f_{7/2}$ and Bi $4f_{5/2}$ of Bi-O bonds, respectively.[9] As seen in Fig.4 (E), in addition to the characteristic peaks of Bi-O, two other relatively weak peaks at 162.1 and 157.3 eV are observed on WBGR that are most likely generated by the Bi-C bond.[14, 39] The C-Bi bonds formation indicates that, when GO is reduced to GR during hydrothermal treatment, most of the oxygen-containing functional groups (e.g., -COOH and -OH) disappear, therefore, the π electrons on C atom cannot bond with the others to form a delocalized large π bond.[40] Consequently, the remaining unpaired π electrons on C atom should easily bond with Bi species on the $Bi_2O_2CO_3$ surface during the hydrothermal reduction treatment (Scheme 2).

Optical Characterization

The optical properties of the photocatalysts are probed using UV-vis diffuse reflectance spectroscopy (Figure S4† of Supporting Information). The bandgap (inset) is obtained from DRS via the MKS equation (i.e., $[\alpha h\nu]^{1/2}$ versus photon energy). Compared to $Bi_2O_2CO_3$ (Eg =3.3 eV) and BGR (Eg =3.13 eV), we observed a red-shift in the visible-light absorption edge for WBGR (Eg =2.88 eV). This phenomenon occurs mainly because the C-Bi bonds are formed.

Photocatalytic Activity

The photocatalytic activity of the as-prepared samples is evaluated by photocatalytic degradation of CBZ under light illumination (Fig. 5). After 180 min, the CBZ concentrations $Bi_2O_2CO_3$ and BGR are 14.09 mg/L and 9.63 mg/L, respectively, with relative low removal rates. Over the WBGR photocatalyst, the CBZ removal is approximately 95.4%, almost complete removal. Fig 5 also reveals that the apparent rate constants (k). For WBGR, k is 2.81×10^{-4} /s and is 8.67 and 4.15 times higher than that of $Bi_2O_2CO_3$ and BGR, respectively.

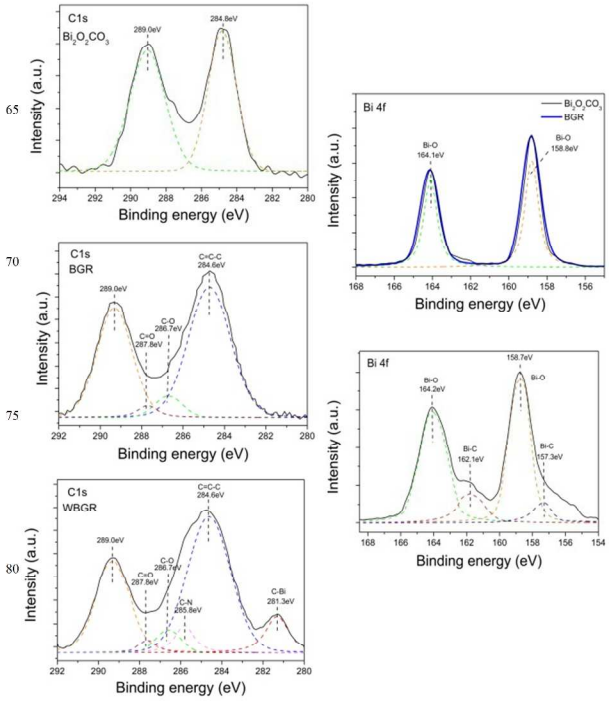

Fig. 4 XPS spectra of the as-prepared samples. **(A).** The C 1s XPS spectra of $Bi_2O_2CO_3$. **(B).** The C 1s XPS spectra of BGR. **(C).** The C 1s XPS spectra of WBGR. **(D).** The Bi 4f XPS spectra of $Bi_2O_2CO_3$ and BGR. **(E).** The Bi 4f XPS spectra of WBGR.

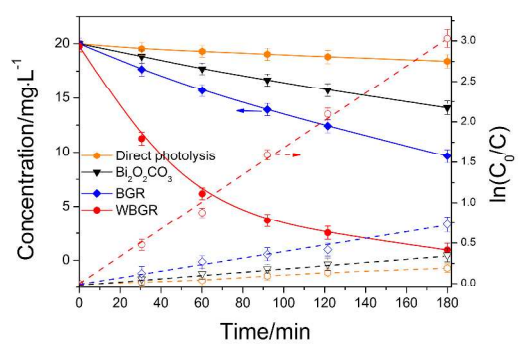

Fig. 5 The degradation efficiency (C/C_0) as a function of elapsed time on $Bi_2O_2CO_3$, BGR and WBGR (solid line) and the apparent pseudo first order rate constants (k) as a function of elapsed time on $Bi_2O_2CO_3$, BGR and WBGR during the CBZ photocatalytic experiment (dash line).

The apparent quantum efficiency, Charge separation yield and electron transfer dynamics

The superior photocatalytic activity of WBGR is mainly caused by the GR shell encapsulation because the interfaces contact area is maximized, forming C-Bi chemical bonds. To verify that the GR shell interface benefits the interfacial charge transfer and charge separation over WBGR, charge separation yield, the apparent quantum efficiency (Φ) and quenching factor as well as

electron transfer dynamic is investigated using EPR, PL and TRPL. As observed in Fig. 6A, EPR is utilized to track the photoexcited trapped hole-centers (O^-).[33, 41, 42] A simulated O^- spectrum is displayed for comparison with an experimental spectrum acquired from $Bi_2O_2CO_3$ microspheres after 30 min of UV irradiation under high vacuum. The photo-excited state of the $Bi_2O_2CO_3$ is described by eq (2-4). After separation and follow by persistent trapping of the photo-excited holes and electrons, the O^- center and the trap state of electrons (Bi^{n+}) are formed.

$Bi_2O_2CO_3 + h\nu \rightarrow e^-_{CB} + h^+_{VB}$ (2)

$h^+_{VB} + O^{2-} \rightarrow O^-$ trapped hole (3)

$e^-_{CB} + Bi^{3+} \rightarrow Bi^{n+}$ trapped electron (n=0, 1, 2) (4)

The corresponding EPR spectrum for BGR reveals that the spin signal for O^- stabilized on BGR is a little stronger than that of $Bi_2O_2CO_3$. Specifically, compared to $Bi_2O_2CO_3$ and BGR, WBGR exhibits much stronger signal for O^- radicals stabilized on the $Bi_2O_2CO_3$ microspheres. This stronger O^- radical signal indicates that the h^+ and e^- are separated efficiently instead of recombination; therefore, more h^+ can react with O^{2-} to generate O^- radicals. However, due to the physicochemical spin characteristics of Bi, Bi^{n+} is difficult to detect via EPR. Therefore, the apparent quantum efficiency is measured to quantitatively analyze the separation of photoexcited hole-electrons pairs. According to eq (1), the apparent quantum efficiency (Φ) for CBZ degradation by $Bi_2O_2CO_3$, BGR and WBGR are 0.30%, 0.63% and 2.62%, respectively, indicating that the quantum efficiency of WBGR is enhanced via GR encapsulating.

Fig. 6B displays the apparent quantum efficiency and quantitative analysis of the persistently trapped photoexcited charges on $Bi_2O_2CO_3$, BGR and WBGR. We defined the spin concentration of the O^- radical as the charge separation yield. Compared to $Bi_2O_2CO_3$ (approximately 1.5×10^{17} spin·g^{-1}), there is a slight increase in the spin concentration of O^- radical for the BGR (approximately 3×10^{17} spin·g^{-1}). The result indicates that some electrons located in the CB or in shallow trap states transfer readily to GR because its excellent electronic conductivity. Consequently, the recombination of photoexcited hole-electron is inhibited and the charge separation yield of BGR increases. However, the contact area between the $Bi_2O_2CO_3$ and GR remains quite limited for BGR. Therefore, the improvement is not significant. For WBGR, the highest charge separation yield of 9.4 $\times 10^{17}$ spin·g^{-1} is observed; simultaneously, the highest quantum efficiency (2.62%) is achieved. This large improvement is attributed to maximized contact area between the $Bi_2O_2CO_3$ cores and GR shells. More of the photoexcited electrons in apparent $Bi_2O_2CO_3$ are transferred to the GR shell than for BGR. In additional, in contrast to the physical absorption in BGR, the interfacial connection between the $Bi_2O_2CO_3$ and GR is achieved by chemical bonds (C-Bi bond) in WBGR (Scheme 1 and 2). This close connection should facilitate ultrafast charges transfer and separation, achieving high charge separation yield with WBGR finally. Meanwhile, the C-Bi bonds formation red shifts the absorption edge of the WBGR, enhancing the light energy ability and utilization to generate more of the excited hole-electron pairs. The lower recombination rate on WBGR is also confirmed using PL spectra. As observed in Fig. 7A, the PL peaks of the as-prepared samples are similar. Specifically, the WBGR exhibits an

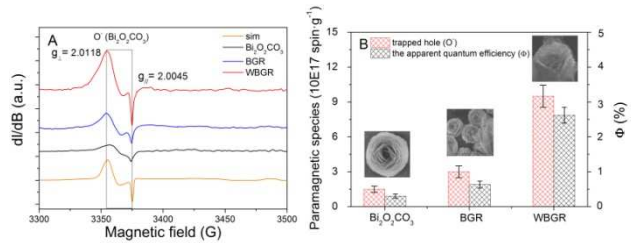

Fig. 6 (A). EPR spectra of O- centers on $Bi_2O_2CO_3$, BGR and WBGR after 30 min light irradiation. **(B).** Quantitative analysis of trapped photoexcited hole (O-) and the apparent quantum efficiency on Bi2O2CO3, BGR and WBGR.

obviously decreased emission signal relative to the $Bi_2O_2CO_3$ and BGR, indicating that there is lower recombination rate on WBGR. To quantify these differences, a quenching factor for each as- prepared sample is obtained by weighting the integrated PL intensity from 250 to 550 nm against that from $Bi_2O_2CO_3$, as follow:[43]

Quenching factor = integrated PL intensity ($Bi_2O_2CO_3$)/integrated PL intensity (samples) (5)

The quenching factor of $Bi_2O_2CO_3$, BGR and WBGR is 1, 1.33 and 4.51, respectively. This result is consistent with the quantitative analysis of the high charge separation yield and the photocatalytic activity mentioned above.

Electron transfer dynamics are key processes contributed to the charge separation yield and photocatalytic activity of WBGR. Therefore, TRPL is introduced to gain further insight into underlying electron transfer dynamics process and their effect on the photocatalytic activity. To quantitatively analyze the PL lifetime based on the TRPL measurement, we can use exponential functions to fit the TRPL curves. Here, two parameters, the fast and slow time constants, are introduced to approximately evaluate the electron transfer kinetics (Fig. 7C).[43]

$$I(t) = \sum_{i=1}^{n} A_i e^{-\tau/\tau_i}$$

As shown in Fig. 7B, all the decay curves are well described by two components of exponential functions. The lifetimes of harvesting excited electrons of $Bi_2O_2CO_3$, BGR, WBGR are 9.83 ns, 8.07 ns and 0.88 ns (fast time constants τ_1) as well as 127.3 ns, 123.9 ns and 118.6 ns (slow time constants τ_2), respectively. In general, some electrons excited to the CB will immediately relax to the bottom of the CB to form polarons. Subsequently, the polarons will react with the holes, generating luminescence emissions. This process of directly forming self-trapped exciton (STE) refers to the fast time constants of luminescence. However, the slow time constant is most likely a result of shallow traps (near the CB of $Bi_2O_2CO_3$) in which the shallow trapped electron would be thermally re-excited to the CB and then relaxed to the bottom of CB. We call this delayed process as indirect STE state, and it generates the slow time constants.[44] The difference between the slow time constants of the as-prepared samples is not obvious. Therefore, the slow component is not affected by GR encapsulation. However, the fast time constant on the WBGR (0.88 ns) is much faster than that of $Bi_2O_2CO_3$ (9.83 ns) or BGR (8.07 ns). Therefore, the fast time component is the dominant process during charge separation. During this process, the electrons transfer from $Bi_2O_2CO_3$ to GR in the form of non-radiative transfer; therefore, the luminescence (radiative transfer)

Table 1. A summary of all performed characterization and the main experiments observation.

Samples	S_{BET} ($m^2 \cdot g^{-1}$)	Bandgap (eV)	Charge separation yield (10^{17}spin·g^{-1})	The apparent quantum efficiency (%)	PL Quenching factor with respect to $Bi_2O_2CO_3$	Fast time constant (ns)	Slow time constant (ns)	The apparent rate constant k ($10^{-5} \cdot s^{-1}$)	The conduction band potential E_{CB} (V vs. NHE)
$Bi_2O_2CO_3$	36.3957	3.30	1.5	0.3	1.0	9.83	127.3	3.24	0.15
Graphene- $Bi_2O_2CO_3$ (BGR)	46.1827	3.13	3.0	0.63	1.33	8.07	123.9	6.77	-0.10
Graphene-wrapped $Bi_2O_2CO_3$ (WBGR)	54.2813	2.88	9.4	2.62	4.51	0.88	118.6	28.4	-0.37

decreases dramatically on WBGR, generating the fastest time constants (0.88 ns). To confirm this conclusion, 5 ns range experiments are performed (Fig. 7D). The luminescence decay (approximately 90% in amplitude) has a time constant of 800 ps. However, the luminescence decay on $Bi_2O_2CO_3$ and BGR are negligible, according to their small amplitude. We attribute this rapid luminescence decay process in WBGR to the ultrafast transfer of the photoexcited electrons via the excellent electronic conductivity of GR and the C-Bi bonds at the connection interface.

The correlation analysis between the fast lifetime constants (τ_1) and C/C_0, charge separation yield and the PL quenching factor are further summarized. Fig. 8 contains a plot of the characteristic lifetime versus the photocatalytic activity, charge separation yield and the quenching factor. A shorter lifetime indicates there is an

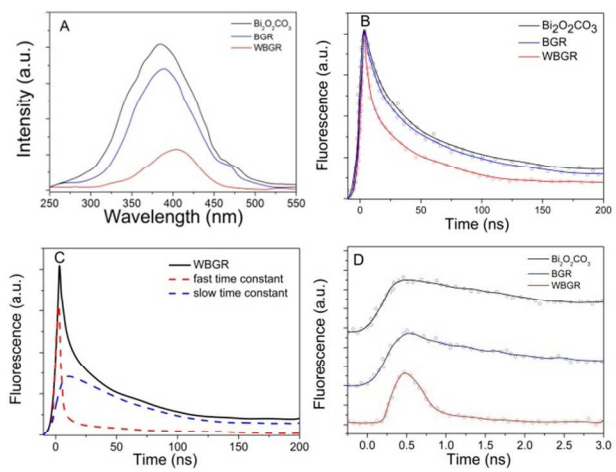

Fig.7 (A). The photoluminescence (PL) spectra on $Bi_2O_2CO_3$, BGR and WBGR. **(B).** Time-resolve fluorescence spectra (TRPL) on $Bi_2O_2CO_3$, BGR and WBGR (200 ns scanning range with an IRF of 2ns). The solid line displays the curve fitting. **(C).** The fast (red) and slow (blue) delay components on WBGR, respectively. **(D).** Time-resolve fluorescence spectra (TRPL) on $Bi_2O_2CO_3$, BGR and WBGR (2.5 ns scanning range with an IRF of 60 ps). The solid line shows the curve fitting.

The correlation analysis between the fast lifetime constants (τ_1) and C/C_0, charge separation yield and the PL quenching factor are further summarized. Fig. 8 contains a plot of the characteristic lifetime versus the photocatalytic activity, charge separation yield and the quenching factor. A shorter lifetime indicates there is an efficient interface for electrons transfer that lowers the recombination rate and raises the charge separation yield (trapped hole $\cdot O^-$). Finally, the photocatalytic activity is improved. By the concept of correlation analysis, the electronic lifetime can be used as a new approach to evaluate the photocatalytic activity of materials.

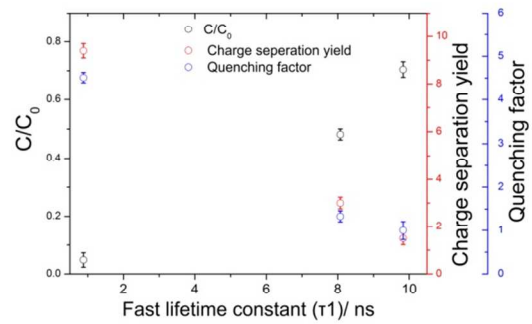

Fig.8 The correlation analysis between fast component lifetime constant (τ_1) and charge separation yield (trapped hole center O^- spin concentration), charge recombination rate (quenching factor), and photocatalytic activity (C/C_0).

Table 1 displays a summary of all performed characterizations and the main experiment observations.

Radical reaction mechanism

To validate the proposed radical reaction mechanism for photocatalytic CBZ degradation over WBGR, several control experiments are performed under UV-vis light,[45] as displayed in Fig. 9A. Fig. 9B displays the PL signal associated with the nitroblue tetrazolium (NBT) from the reaction between NBT and the $\cdot O_2^-$ radicals. As shown in Fig. 9A, when a radical scavenger, such as benzoquinone (BQ) for the $\cdot O_2^-$ radical, is added, the CBZ removal moderately decreases, indicating that the $\cdot O_2^-$ radical may act as reactive oxygen species that participates in the photocatalytic degradation on WBGR. The relative process is displayed in (eq 6-9). Fig S5† displays the MS plots of $Bi_2O_2CO_3$ and WBGR, V_{fb} is calculated from the x intercepts of the linear region. For n-type seminconductor, V_{fb} equals to E_F and is an inherent property of the semiconductor.[43] The MS plots of $Bi_2O_2CO_3$ show that the E_F of $Bi_2O_2CO_3$ is approximately 0.25 V vs. NHE, which is more positive than E_0 ($O_2/\cdot O_2^-$ =-0.28 V vs. NHE); therefore, there is no $\cdot O_2^-$ radical production on $Bi_2O_2CO_3$ (Fig. 9B indicates that the NBT transformation percentage on $Bi_2O_2CO_3$ and BGR is zero). However, the E_F of WBGR is -0.47 V vs. Ag/AgCl (equivalent to -0.27 V vs. NHE), an obviously negative shift compared to that of $Bi_2O_2CO_3$ (0.05 V vs. Ag/AgCl, equivalent to 0.25 V vs. NHE). It is generally accepted that the CB potential is approximately 0-0.2 V more negative than the E_F (Here, we set this value as 0.1 V). Therefore, the negative shift in the E_F of WBGR causes the WBGR E_{CB} to shift from 0.15 V to -0.37 V vs. NHE (more negative than $O_2/\cdot O_2^-$ = -0.28 V vs. NHE). Consequently, the $\cdot O_2^-$ radical is generated on WBGR (Fig. 9B demonstrate that the NBT transformation

percentage on WBGR is 88%) and participates in the photocatalytic reaction (eq 6-9). We know that the calculated work function of GR is -4.42 eV vs. vacuum (equivalent to the E_F of GR, -0.08 V vs. NHE), [46] which is more negative than the E_F of $Bi_2O_2CO_3$; therefore, the photoexcited electrons transfer occurs from the $Bi_2O_2CO_3$ to GR when they are in contact during the photocatalytic experiment. Consequently, the accumulation of electrons and the electronic interactions in the $Bi_2O_2CO_3$-GR system inevitably causes a shift of the apparent Fermi level (E_F^*) in the $Bi_2O_2CO_3$-GR system.[47, 48] The results are similar with Gao et al. and Zhu et al. reports, in which the negative shift in the Fermi level causes the E_{CB} of G-BWO shift from 0.16 V to -0.36 V and from 0.09 V to -0.30 V in the graphene-Bi_2WO_6 system, respectively. [13, 49]

In additional, when a radical scavenger for ·OH is added, the CBZ conversion is significantly hindered (eq 9). In particular, CBZ removal of values down to 27% is observed when a scavenger for holes (AO) is added, meaning that holes and subsequent generated ·OH are the dominant oxidation species during the photocatalytic process (eq (10-12)) with WBGR. The $\cdot O_2^-$ radical, the ·OH radical and holes participate in the photocatalytic degradation over WBGR; therefore, the photocatalytic activity is enhanced significantly. The entire radical reaction mechanism is presented as follows:

$$e^- + O_2 \rightarrow \cdot O_2^- \quad (6)$$

$$\cdot O_2^- + H_2O \rightarrow \cdot HO_2 + OH^- \quad (7)$$

$$\cdot HO_2 + H_2O \rightarrow H_2O_2 + \cdot OH \quad (8)$$

$$H_2O_2 + \cdot O_2^- \rightarrow \cdot OH + OH^- + O_2 \quad (9)$$

$$\cdot OH + CBZ \rightarrow \text{oxidation products} \quad (10)$$

$$h^+ + CBZ \rightarrow \text{oxidation products} \quad (11)$$

$$h^+ + H_2O \rightarrow \cdot OH + H^+ \quad (12)$$

Conclusions

In summary, we successfully demonstrated that the remarkable enhancement of quantum efficiency is achieved via maximizing the contact area between graphene and $Bi_2O_2CO_3$ using graphene encapsulation. Consequently, WBGR displays an excellent photocatalytic activity in the degradation of CBZ benefited from the hierarchical feature of $Bi_2O_2CO_3$ and the formation of C-Bi bonds interface. This work opens up a new application of graphene as a chemical bonds connective shell in the ultrafast electrons transfer dynamics of the photocatalysts. Therefore, graphene-wrapped functional nanoparticles may have a great potential in the field of environmental and energy storage as well as conversion, such as water treatment, green catalysis, fuel cells and carbon dioxide conversion.

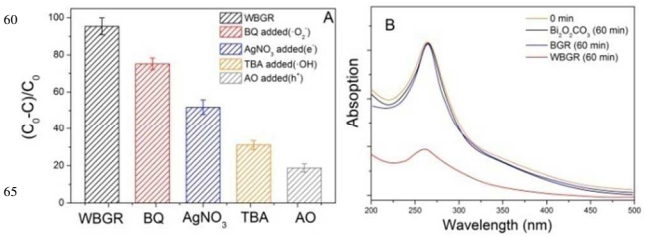

Fig. 9 **(A)** Radicals control experiments using different radical scavengers on WBGR during the CBZ photocatalytic degradation; Benzoquinone (BQ) as scavenger for superoxide radicals ($\cdot O_2^-$); $AgNO_3$ as scavenger for electrons; Tert-butyl alcohol (TBA) as scavenger for hydroxyl radicals (·OH); ammonium oxalate (AO) for holes; **(B)**. UV-vis absorption spectra of NBT on $Bi_2O_2CO_3$, BGR and WBGR.

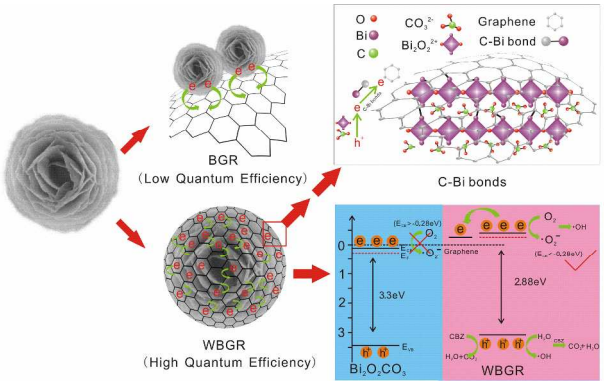

Scheme 2 Schematic illustration of enhanced quantum efficiency and radicals' reaction mechanism on WBGR

Acknowledgements

This work was partially supported by the fundamental research project of the Science and Technology Commission of Shanghai (11JC1412600), New Century Excellent Talents in University (NCET-11-0391),
National Natural Science Foundation of China(21246001, 51278356, 51138009) and by the National Key Technology R&D Program of China (NO. 2012BAJ25B02).

References

1. D. Y. Li, Y. G. Zhang, Y. L. Zhang, X. F. Zhou and S. J. Guo, *J.Hazard.Mater*, 2013, 258, 42-49.
2. R. G. Li, F. X. Zhang, D. G. Wang, J. X. Yang, M. R. Li, J. Zhu, X. Zhou, H. X. Han and C. Li, *Nat.Commun*, 2013, 4.
3. S. M. Sun, W. Z. Wang and L. Zhang, *J.Phys.Chem.C*, 2013, 117, 9113-9120.
4. G. H. Tian, Y. J. Chen, W. Zhou, K. Pan, Y. Z. Dong, C. G. Tian and H. G. Fu, *J.Mater.Chem*, 2011, 21, 887-892.
5. X. Zhao, J. H. Qu, H. J. Liu and C. Hu, *Environ.Sci.Technol*, 2007, 41, 6802-6807.
6. J. Jiang, K. Zhao, X. Y. Xiao and L. Z. Zhang, *J.Am.Chem.Soc*, 2012, 134, 4473-4476.
7. Y. N. Wang, K. J. Deng and L. Z. Zhang, *J.Phys.Chem.C*, 2011, 115, 14300-14308.
8. L. Ye, J. Liu, C. Gong, L. Tian, T. Peng and L. Zan, *ACS Catal*, 2012, 2, 1677-1683.
9. F. Dong, Y. J. Sun, M. Fu, W. K. Ho, S. C. Lee and Z. B. Wu, *Langmuir*, 2012, 28, 766-773.
10. L. Chen, R. Huang, S. F. Yin, S. L. Luo and C. T. Au, *Chem.Eng.J*,

2012, 193, 123-130.
11. S. J. Peng, L. L. Li, H. T. Tan, Y. Z. Wu, R. Cai, H. Yu, X. Huang, P. N. Zhu, S. Ramakrishna, M. Srinivasan and Q. Y. Yan, *J.Mater.Chem.A*, 2013, 1, 7630-7638.
12. P. Madhusudan, J. R. Ran, J. Zhang, J. G. Yu and G. Liu, *Appl.Catal.B-Environ*, 2011, 110, 286-295.
13. E. P. Gao, W. Z. Wang, M. Shang and J. H. Xu, *Phys.Chem.Chem.Phys*, 2011, 13, 2887-2893.
14. J.-Y. Liu, Y. Bai, P.-Y. Luo and P.-Q. Wang, *Catal.Commun*, 2013.
15. K. S. Novoselov, A. K. Geim, S. V. Morozov, D. Jiang, Y. Zhang, S. V. Dubonos, I. V. Grigorieva and A. A. Firsov, *Science*, 2004, 306, 666-669.
16. S. Stankovich, D. A. Dikin, G. H. B. Dommett, K. M. Kohlhaas, E. J. Zimney, E. A. Stach, R. D. Piner, S. T. Nguyen and R. S. Ruoff, *Nature*, 2006, 442, 282-286.
17. N. Zhang, Y. H. Zhang and Y. J. Xu, *Nanoscale*, 2012, 4, 5792-5813.
18. M. Q. Yang and Y. J. Xu, *Phys.Chem.Chem.Phys*, 2013, 15, 19102-19118.
19. Y. H. Zhang, Z. R. Tang, X. Z. Fu and Y. J. Xu, *ACS Nano*, 2010, 4, 7303-7314.
20. Y. H. Zhang, Z. R. Tang, X. Fu and Y. J. Xu, *ACS Nano*, 2011, 5, 7426-7435.
21. Y. H. Zhang, N. Zhang, Z. R. Tang and Y. J. Xu, *ACS Nano*, 2012, 6, 9777-9789.
22. Q. J. Xiang, J. G. Yu and M. Jaroniec, *Chem.Soc.Rev*, 2012, 41, 782-796.
23. L. M. Dai, *Acc.Chem.Res*, 2013, 46, 31-42.
24. J. Liu, H. Bai, Y. Wang, Z. Liu, X. Zhang and D. D. Sun, *Adv.Funct.Mater*, 2010, 20, 4175-4181.
25. P. Madhusudan, J. G. Yu, W. G. Wang, B. Cheng and G. Liu, *Dalton T*, 2012, 41, 14345-14353.
26. J. Zhang, Z. P. Zhu, Y. P. Tang and X. L. Feng, *J.Mater.Chem.A*, 2013, 1, 3752-3756.
27. H. I. Kim, G. H. Moon, D. Monllor-Satoca, Y. Park and W. Choi, *J.Phys.Chem.C*, 2012, 116, 1535-1543.
28. J. S. Lee, K. H. You and C. B. Park, *Adv. Mater*, 2012, 24, 1084-1088.
29. M. Q. Yang, B. Weng and Y. J. Xu, *Langmuir*, 2013, 29, 10549-10558.
30. S. Q. Liu, Z. Chen, N. Zhang, Z. R. Tang and Y. J. Xu, *J.Phys.Chem.C*, 2013, 117, 8251-8261.
31. Z. Chen, S. Q. Liu, M. Q. Yang and Y. J. Xu, *ACS Appl.Mater.Inter*, 2013, 5, 4309-4319.
32. A. Cao, Z. Liu, S. Chu, M. Wu, Z. Ye, Z. Cai, Y. Chang, S. Wang, Q. Gong and Y. Liu, *Adv.Mater*, 2010, 22, 103-106.
33. M. D'Arienzo, J. Carbajo, A. Bahamonde, M. Crippa, S. Polizzi, R. Scotti, L. Wahba and F. Morazzoni, *J.Am.Chem.Soc*, 2011, 133, 17652-17661.
34. B. Subash, B. Krishnakumar, M. Swaminathan and M. Shanthi, *Langmuir*, 2013, 29, 939-949.
35. F. Dong, W. K. Ho, S. C. Lee, Z. B. Wu, M. Fu, S. C. Zou and Y. Huang, *J.Mater.Chem*, 2011, 21, 12428-12436.
36. F. Dong, S. C. Lee, Z. B. Wu, Y. Huang, M. Fu, W. K. Ho, S. C. Zou and B. Wang, *J.Hazard.Mater*, 2011, 195, 346-354.
37. Y. Wang, Y. Y. Wen, H. M. Ding and Y. K. Shan, *J.Mater.Sci*, 2010, 45, 1385-1392.
38. H. Liu, X. Dong, X. Wang, C. Sun, J. Li and Z. Zhu, *Chem.Eng.J*, 2013.
39. F. Meng, J. Li, S. K. Cushing, M. Zhi and N. Wu, *J.Am.Chem.Soc*, 2013, 135, 10286-10289.
40. C. Nethravathi and M. Rajamathi, *Carbon*, 2008, 46, 1994-1998.
41. N. M. Dimitrijevic, E. Rozhkova and T. Rajh, *J.Am.Chem.Soc*, 2009, 131, 2893-2899.
42. N. Siedl, S. O. Baumann, M. J. Elser and O. Diwald, *J.Phys.Chem.C*, 2012, 116, 22967-22973.
43. R. Sellappan, J. Sun, A. Galeckas, N. Lindvall, A. Yurgens, A. Kuznetsov and D. Chakarov, *Phys.Chem.Chem.Phys.*, 2013.
44. K. Wakabayashi, Y. Yamaguchi, T. Sekiya and S. Kurita, *J.Lumin*, 2005, 112, 50-53.
45. Y. H. Zhang, N. Zhang, Z. R. Tang and Y. J. Xu, *Chem.Sci*, 2013, 4, 1820-1824.
46. P. Roy, A. P. Periasamy, C. T. Liang and H. T. Chang, *Environ.Sci.Technol*, 2013, 47, 6688-6695.
47. V. Subramanian, E. E. Wolf and P. V. Kamat, *J.Am.Chem.Soc*, 2004, 126, 4943-4950.
48. A. Kongkanand and P. V. Kamat, *ACS Nano*, 2007, 1, 13-21.
49. Z. Sun, J. Guo, S. Zhu, L. Mao, J. Ma and D. Zhang, *Nanoscale*, 2014, 6, 2186-2193.